Structural Dynamics Effects on Spacecraft Attitude Control: A Modal Analysis Modeling Approach

3. Structural Dynamics Effects on Spacecraft Attitude Control: A Modal Analysis Modeling Approach

3.1. Introduction

Flexible spacecraft are dynamic systems that provide a rich area for research, especially in the design of spacecraft control systems and their interaction with the spacecraft's structure. These systems are characterized by multiple dynamic modes that must be addressed separately or as an integrated system to completely understand and control the spacecraft's behavior.

3.2. Importance of Spacecraft Modal Analysis

Spacecraft modal analysis is crucial for understanding how these dynamic modes interact and how they can be controlled to meet specific system performance requirements and design constraints. This analysis helps achieve the desired level of interaction between the spacecraft's flexible and rigid components, which is essential for optimal performance.

3.3. Structural Components of Spacecraft

The spacecraft structure typically consists of two main parts: the main body and the flexible appendages. The main body contains components like the payload and control hardware and is designed to be quasi-rigid to minimize vibrations during crucial missions. On the other hand, flexible appendages, such as parabolic antennas and solar arrays, are lightweight to reduce overall mass but introduce additional dynamic challenges. These appendages can oscillate due to external forces, leading to complex vibrational dynamics that disturb the spacecraft's attitude control systems.

To effectively manage and control these dynamics, spacecraft flexibility is modeled at various levels of complexity:

Vibration Analysis of Flexible Appendages: This analysis studies the vibration characteristics and dynamics of components such as solar panels and antennas. Accurate analysis of these flexible appendages is crucial for understanding their impact on the overall system's performance and stability [19, 20].

Attitude Maneuver and Vibration Analysis: At this level, the analysis focuses on how the satellite's attitude maneuvers and control are influenced by the vibrations of its flexible appendages, such as solar panels and antennas. This integrated approach combines attitude control dynamics with the dynamic response of these vibrating components, providing a comprehensive understanding of their coupled effects on the overall system's behavior [21, 22].

Orbital Motion and Comprehensive Dynamics: This advanced level of modeling contains both the satellite's attitude maneuvers and the vibrational dynamics of its flexible appendages. Integrating these elements provides a comprehensive and holistic understanding of the spacecraft's intricate behavior and motion characteristics while in orbit, accounting for the complex interplay between various subsystems and their impact on the overall system dynamics [23, 24].

General Motion Analysis: At the most comprehensive level, this analysis encompasses all aspects of the satellite's motion, including translational (orbital), rotational (attitude), and

vibrational dynamics. Integrating these diverse motion characteristics offers detailed and extensive insights into the spacecraft's complex behavior and dynamics under various operational conditions and external disturbances [27].

This chapter examines specific structural vibrations. To illustrate the analysis of spacecraft motion, Fig 3.1 depicts a spacecraft configuration consisting of a main body and two solar arrays. By studying the dynamics of such a configuration, we can understand the behavior of flexible spacecraft in practical scenarios.

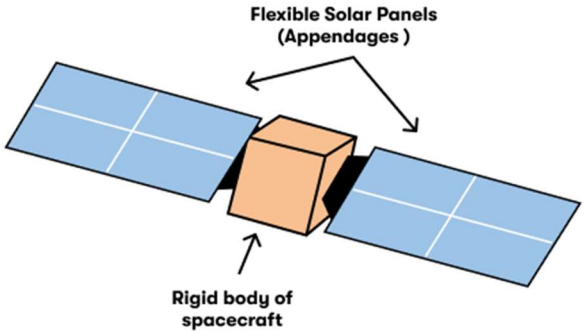

Fig 3.1: Flexible spacecraft with solar arrays.

Based on the typical satellite flexible modes that interact with control design, vibrations in a spacecraft are not only introduced from flexible appendages but also from its own internal dynamics. The rigid hub of a spacecraft is not entirely rigid as it accommodates the propellant tanks. Any large manoeuvres or disturbances associated with operations can lead to slosh dynamics, further amplifying the oscillations of the appendages [26] Dynamic disturbances such as liquid slosh, depicted in Fig 3.2; To model the mechanical effects of liquid slosh, the propellant can be represented as a combination of fixed and slosh masses [18,19].

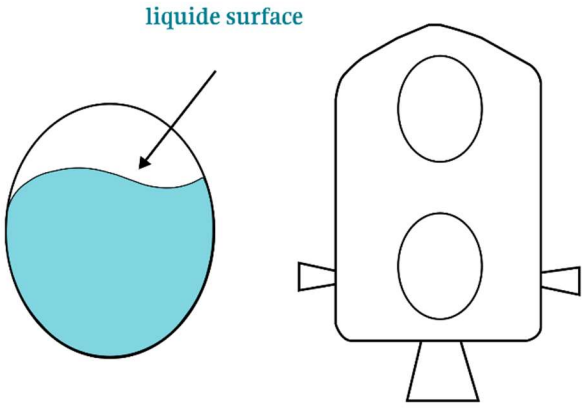

Fig 3.2: A spacecraft with a liquid propellant tank.

Based on the studies above, this section researches flexible spacecraft with rotating appendages and platforms while considering the influence of the rotation and vibration of flexible solar panels and the influence of rigid rotating payload. This section aims to solve the attitude control problem of this kind of complex spacecraft.

3.4. Description of Flexible Spacecraft with Rotating Appendages

To analyze the dynamics of a wide range of flexible spacecraft, we model the system as a rigid central hub representing the main body, with two rigidly attached flexible appendages, as illustrated in Fig 3.3. We consider a three-axis rotation maneuver performed on the spacecraft, driven by torque control applied at the hub. It is assumed that this maneuver excites the flexible appendages, causing them to vibrate without shifting the overall center of mass of the spacecraft. Consequently, both appendages exhibit identical deflection profiles. These elastic transverse deformations are restricted to the plane, which is perpendicular to the axis of rotation, as shown in Fig 3.1. The solar panels attached to the sides of the satellite act as flexible appendages, and there are numerous modeling approaches available to characterize their behavior accurately.

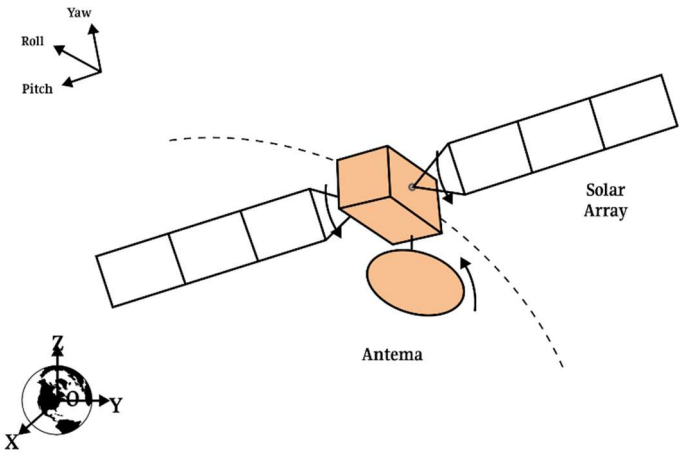

Fig 3.3: Model of the reference spacecraft with Body axes.

In another approach, we can consider the spacecraft as a central rigid body with multiple flexible appendages, as depicted in Fig 3.4. These flexible appendages are connected to the central platform through various types of connectors, including fixed rigid connections, hinged joints (both rigid and flexible), actuated motors, or other damping structures. This modeling approach allows for a more comprehensive representation of the spacecraft's configuration, accounting for the interaction between the central body and the dynamics of multiple flexible components such as solar arrays, antennas, or deployable structures.

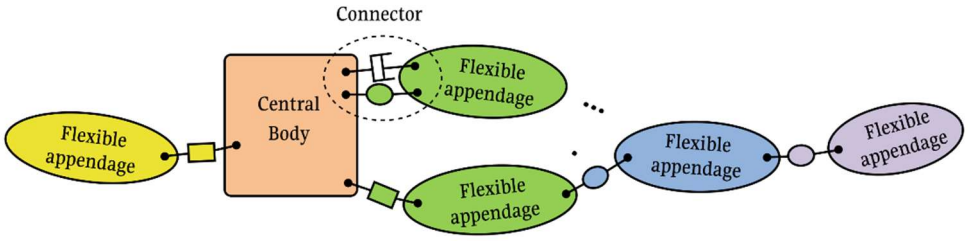

Fig 3.4: Topology configuration of flexible spacecraft.

After discussing the topology configuration of a flexible spacecraft, it is essential to delve into the description of motion in order to formulate the equations of motion.

3.4.1. Description of Motion

To formulate the equations of motion accurately, it is necessary to introduce appropriate coordinate systems, as depicted in Fig 3.5 and referenced in [10].

(1) The frame OXYZ is considered an inertial frame with its origin fixed at point O.

(2) The frame o x y z is identified as a body frame that aligns with the principal axes of the platform and has its origin at the mass center of the platform. Given that the platform is treated as a rigid body, the movement of the Spacecraft can be explained through the translations and rotations of the o x y z coordinate system concerning the OXYZ coordinate system.

(3) The frame $o_s\ x_s\ y_s\ z_s$ is defined as a floating frame that is associated with the flexible appendage in its undeformed state, having its origin at the hinge point o_s. This particular coordinate system is utilized to characterize the rigid motion of the flexible body in relation to the inertial space, encompassing translations and rotations. Generally, the origin is positioned at the junction between the flexible body and the spacecraft platform. The elastic deformation of the flexible body is delineated by the relative position of the flexible body and its body coordinate system, and the flexible body can be discrete by the hypothetical mode method or the finite element method.

(4) The frames $o_{e,I}\ x_{e,i}\ y_{e,i}\ z_{e,i}$ (i = 1,2,…,N) is the local coordinate of the i-th element of the appendage, whose origin is at the mass center $o_{e,i}$ N denotes the total number of elements.[10]

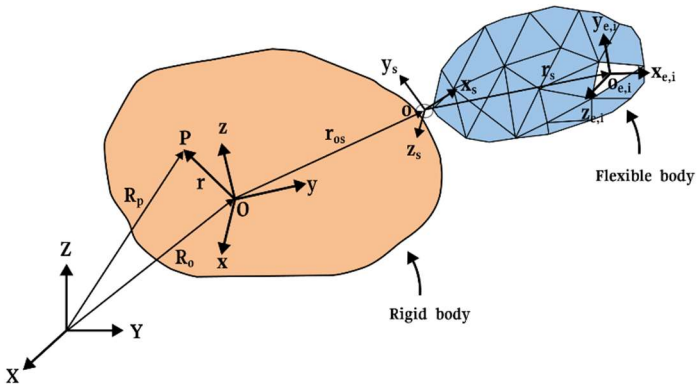

Fig 3.5: Motion description of flexible spacecraft based on the hybrid coordinate method.

After describing the motion, we can discuss model simplification. This section focuses on simplifying models for spacecraft with flexible appendages, such as solar panels and fuel sloshing.

3.4.2. Model of Spinning Appendage

There are two forms of motion for rotating structures: rotations relative to the spacecraft platform and elastic vibration, which can be excited by the platform's motion or the environment. Depending on the configuration and motion characteristics of components such as solar wings, antennas, and other structures, the system can be simplified into a combined structural model that consists of rotating flexible beams and beam-plate elements.

Spinning flexible beam

Considering the solar wing as an example, the fundamental assumptions for simplifying the model (as illustrated in Fig 3.6) can be presented as follows:

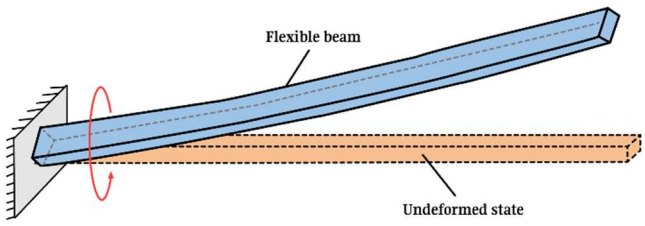

Fig 3.6: Flexible spinning beam model.

In this simplified model, several factors are not taken into consideration. Let's discuss the most important ones:

- **Ignored influence of connecting structures**: The model does not consider the impact of connecting structures, such as motors and slip rings, between the solar wing and the spacecraft.
- **Ignored the impact of spacecraft platform motions:** This model considers only the influence of rotation on the solar wing. Rigid motions in other directions of the spacecraft platform that could affect the rigidity of the solar wing are ignored.
- **Ignored the influence of solar cells and circuits:** The model does not take into account the influence of the solar cells and circuits on the system's rigidity. [10]

Spinning flexible smart beam

Additionally, a piezoelectric structure is integrated onto the flexible beam as an active vibration control actuator, simplifying it to a spinning flexible smart beam, as shown in Fig. 3.7.

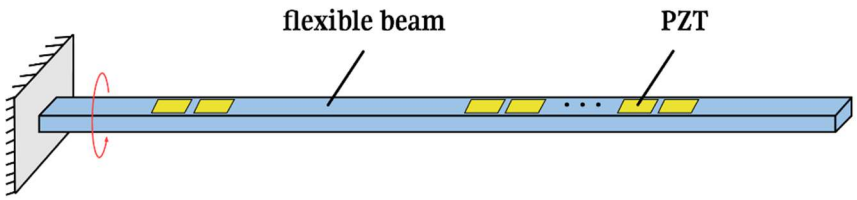

Fig 3.7: Spinning flexible smart beam.

Beam-plate combined structure mode

For a flexible appendage like a solar wing, where one dimension (e.g. thickness) is significantly smaller than the other two dimensions (length and width), the structure can be simplified to a spinning combined beam and thin plate configuration, as depicted in Fig 3.8.

The root of the appendage is considered fixed, with the only permitted degree of freedom being rotation along the intended unfolding direction.

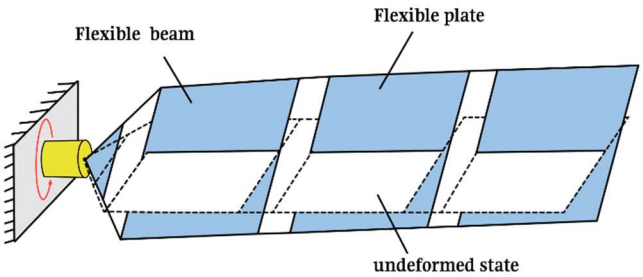

Fig 3.8: Spinning beam-plate combined structure model.

3.4.3. Simplified Model of Spinning Appendage

Based on the configurations of flexible spacecraft, such spacecraft can be simplified as systems consisting of a central body with one or more flexible appendages attached, as illustrated in Fig. 3.9.

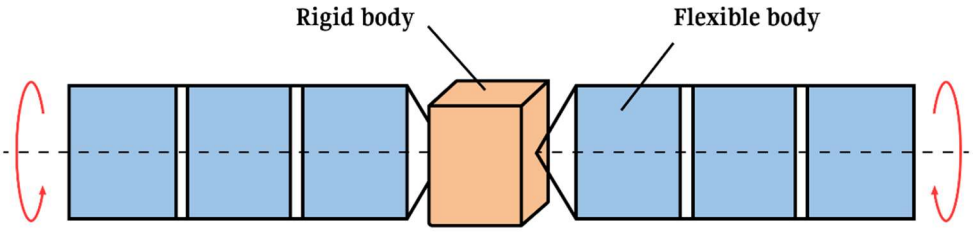

Fig 3.9: Rigid-flexible coupling model of flexible spacecraft with rotating structures.

The basic assumptions for model simplification are as follows:

(1) The central body, representing the spacecraft platform, is simplified as a rigid body capable of unrestricted rotations and translations in the inertial reference frame.

(2) Each appendage is simplified as a flexible body, which can only rotate relative to the platform. The translational degrees of freedom at the hinge point connecting the appendage to the platform are constrained.

(3) Nonlinear factors such as gaps and friction at the connection between the platform and appendages are ignored.

(4) The elastic deformations are assumed to be small, satisfying linear conditions. The material properties of the system components are considered elastic and constant.

(5) The overall system's center of mass is assumed to remain unchanged. [10]

3.5. Modeling of Solar Panels

Although the structural modeling techniques described in this chapter apply to any non-rigid appendage attached to a solid body, we will concentrate on the structural dynamics of solar panels, which are common to almost all types of satellites. Our task is to create a simplified model that adequately represents the real structure and is easy to use for design purposes.

3.5.1. Classification of Techniques

There exist four basic modeling techniques:

(1) Distributed parameter modeling;

(2) Discrete parameter modeling;

(3) N-body modeling;

(4) Finite element modeling. A short conceptual explanation of these techniques follows.

In our case, we use a discrete model consisting of a rigid body and two symmetrical panels, each modeled by a single mass m, reproduced from Williams (1976) with permission from C. G. Williams. For the modeling, we employ the Lagrangian equations for one-mass modeling.

3.5.2. The Lagrange Equations and One-Mass Modeling

The Lagrange Equations and One-Mass Modeling provide a fundamental introduction to structural dynamics. In this simple example, we will solve the dynamic equations for the discrete model shown in Fig 3.10. This model consists of a rigid body with two symmetrical panels, each modeled as a single mass. The analysis will demonstrate how Lagrangian equations can be applied to capture the essential dynamics of such flexible structures.

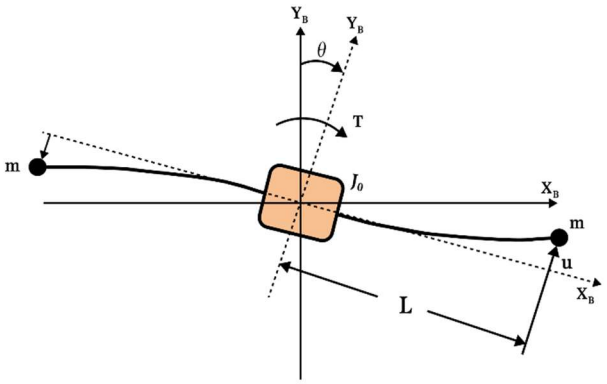

Fig 3.10: Discrete model consisting of a rigid body and two symmetrical panels, each modeled by a single mass **m.**

Attached to the rigid body are modeled by a single discrete mass **m**, positioned at a distance **L** from the center of mass (cm) of the rigid body. The moment of inertia of the rigid body is $\mathbf{J_o}$. A torque **T** is applied about the axis of rotation, thus exciting only the antisymmetric elastic mode. (With an additional force applied along the $\mathbf{Y_B}$ body axis, the symmetric elastic mode will also be excited; this model is not analyzed in the present example.) Since the panel is not rigid, a deformation u with respect to the rigid-body axis is to be anticipated. [11]

The mass m will experience two motions:

(1) a motion 0 with the rigid body, with linear velocity; $\dot{\boldsymbol{\theta}}\boldsymbol{L}$ and

(2) a deformation u from the rigid-body axis $\mathbf{X_B}$, with velocity $\dot{\boldsymbol{u}}$.

For small deformations, both velocities will be collinear; hence the mass m will have a velocity

$$v = u + L\dot{\theta} \qquad (3.1)$$

We shall solve this example by using Lagrange's method. Thus, the kinetic and potential energies $\mathbf{E_k}$ and $\mathbf{E_p}$ are to be written for the entire system, including the two panels (represented by two masses **m)** and the rigid body (represented by its moment of inertia $\mathbf{J_o}$):

$$E_k = \frac{1}{2}J_0\dot{\theta}^2 + 2\left(\frac{1}{2}mv^2\right) \tag{3.2}$$

Together with Eq.3.1, we have

$$E_k = \frac{1}{2}J_0\dot{\theta}^2 + m(u + L\dot{\theta})^2 \tag{3.3}$$

And

$$E_p = 2\left[\frac{u^2}{2}k\right] \tag{3.4}$$

We shall also define a dissipation function D, proportional to half the rate at which energy is dissipated. Taking into account both panels, we have

$$D = 2\left(\frac{\dot{u}^2}{2}k_d\right) \tag{3.5}$$

where **Kd** is the mechanical dissipative constant. The most general form of Lagrange's equations is

$$\frac{d}{dt}\left(\frac{\partial E_k}{\partial \dot{q}_i}\right) + \frac{\partial E_k}{\partial q_i} + \frac{\partial E_p}{\partial q_i} + \frac{\partial D}{\partial \dot{q}_i} = Q_i \quad (i=1,\ldots\ldots,n), \tag{3.6}$$

where the qi are generalized coordinates and Qi denotes the generalized forces or torques acting on the; station. Lagrange's equations for this example are as follows:

$$\frac{\partial E_k}{\partial \dot{\theta}} = J_0\dot{\theta} + 2mL(\dot{u} + L\dot{\theta}) \tag{3.7}$$

$$\frac{d}{dt}\left(\frac{\partial E_k}{\partial \dot{\theta}}\right) = J_0\ddot{\theta} + 2mL(\dot{u} + L\ddot{\theta}) = (J_0 + 2mL^2)\ddot{\theta} + 2mL\dot{u} \tag{3.8}$$

$$\frac{\partial E_k}{\partial \dot{u}} = 2m(\dot{u} + L\dot{\theta}) \tag{3.9}$$

$$\frac{d}{dt}\left(\frac{\partial E_k}{\partial \dot{u}}\right) = 2m(\dot{u} + L\ddot{\theta}) \tag{3.10}$$

$$\frac{\partial E_P}{\partial u} = 2uK \tag{3.11}$$

$$\frac{\partial D}{\partial \dot{u}} = 2\dot{u}k_d \tag{3.12}$$

$$\frac{\partial E_k}{\partial \theta} = \frac{\partial E_k}{\partial u} = \frac{\partial E_P}{\partial \theta} = \frac{\partial D}{\partial \dot{\theta}} = \frac{\partial D}{\partial u} = 0 \tag{3.13}$$

From Eq.3.7 and Eq.3.13 the following equations follow:

$$(J_0 + 2mL^2)\ddot{\theta} + 2mL\dot{u} = T \tag{3.14}$$

$$m\ddot{u} + K_d\dot{u} + ku = -mL\ddot{\theta} \tag{3.15}$$

In Eq.3.14, $\boldsymbol{J_o}$ is the moment of inertia of the rigid body. We shall denote by $\boldsymbol{J_p = mL^2}$ the moment of inertia of one of the two (panel) masses about the cm. Let us define $\boldsymbol{J = J_o + 2mL^2}$. This is the moment of inertia of the entire system, including the two panels.

With this definition Eq.3.14 can be rewritten as:

$$J\ddot{\theta} + 2mL\ddot{u} = T \tag{3.14'}$$

Where $J = J_o + 2mL^2 = J_0 + 2\,J_P$

Equations 3.14 and 3.15 are both linear ordinary differential equations, so they can be solved by Laplace transformations. Simple algebraic manipulation leads to the final solution for θ**(s)** as a transfer function in the Laplace domain ("s" is the Laplace variable) :

$$\frac{\theta(s)}{T(s)} = \frac{1}{j_0 s^2} \cdot \frac{s^2 + \frac{K_d}{m}s + \frac{K}{m}}{s^2 + \frac{J\,K_d}{J_0\,m}s + \frac{J\,K}{J_0 m}} = \frac{1}{J_0 s} \cdot \frac{s^2 + 2\xi\cdot\sigma\cdot s + \sigma^2}{s^2 + 2\xi_s\cdot\sigma_s\cdot s + \sigma_s^2} \tag{3.16}$$

Let us define as $\omega = \sqrt{\boldsymbol{K/m}}$ the cantilever natural frequency of the panel, and let $\xi = (K_d/2)\sqrt{1/Km}$ be its damping coefficient. We label this modal system frequency ω_s, and set $\omega_s = \sqrt{J/J_0}\,\omega$ is the damping coefficient of the denominator pole. The higher the ratio, the higher the modal frequency ω_s and the damping coefficient ξ_s.

According to these definitions, $\omega_s > \omega$ and also $\xi_s > \xi$, From the automatic control perspective.

3.6. Modeling of Liquid Slosh

With today's very large satellite structures, a substantial mass of fuel is necessary to place them into orbit and perform orbit corrections. The mass of fuel contained in the tanks of a geosynchronous satellite amounts to approximately 40% of its total initial mass. When the fuel containers are only partially filled and under translational acceleration, large quantities of fuel move uncontrollably inside the tanks and generate the sloshing effect.

The dynamics of motion of the fuel interact with the solid-body and appendage dynamics of the spacecraft. This interaction of sloshing can produce attitude instability. Several methods have been employed to reduce the effect of sloshing, such as introducing baffles inside the tanks or dividing a large container into several smaller ones.

3.6.1. Basic Assumptions

Modeling of the sloshing phenomenon was initiated in the early sixties. The models of sloshing motion presented in Abramson (1961) have not changed much over the years. An exact analytical model of fluid oscillatory motion inside a moving container is extremely difficult. in fact, impossible. After making some simplifying assumptions, reasonably adequate models have been obtained that are in good agreement with experimental results.

These assumptions include:

(a) small displacements, velocities, and slopes of the liquid-free surfaces;

(b) a rigid tank;

(c) a non-viscous liquid; and

(d) an incompressible and homogeneous fluid.

With these assumptions, the sloshing dynamics model can be written using an infinite number of small masses. The results obtained with such models must be checked against experimental measurements.

In our case, we use mechanical models for pendulum and spring-mass analogies to the sloshing problem, reproduced from Abramson (1966). And for writing the dynamics equations of motion, we use a model adapted from Bryson (1983) with permission from the American Astronautical Society. Well, for the modeling, we use the One-Vibrating Mass Model [11].

3.6.2. One-Vibrating Mass Model

A basic explanation of the sloshing effect follows. The fuel tank is under the action of a force **F**. The nonmoving parts of the container are concentrated in the mass $\mathbf{M_0}$, which is located at the center of mass of the entire system. The moment of inertia about the center of mass is J_0. As a consequence of the applied force, an acceleration $\mathbf{g} = F / (Mo + m)$ will act on the spacecraft. The moving mass m in the container experiences an acceleration component in a direction opposite to the force **F**.

As shown in Fig 3.11 and as is well known, the mass-spring analogy is related to the pendulum analogy, in which the oscillation frequency of the mass-spring.

$$\omega_{osc} = \sqrt{k/m} \tag{3.17}$$

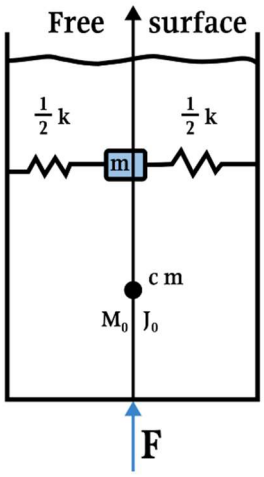

Fig 3.11: Simple mechanical models for pendulum and spring-mass analogies to the sloshing problem.

With m is the equivalent mass m, and **k** is the equivalent spring constant. These parameters depend on the shape and other geometrical parameters of the container, the characteristics of the fluid. And we have also that $\mathbf{k} \approx \mathbf{g} = F/(M_0 + m)$ and that **k** is proportional to the applied force F**.**

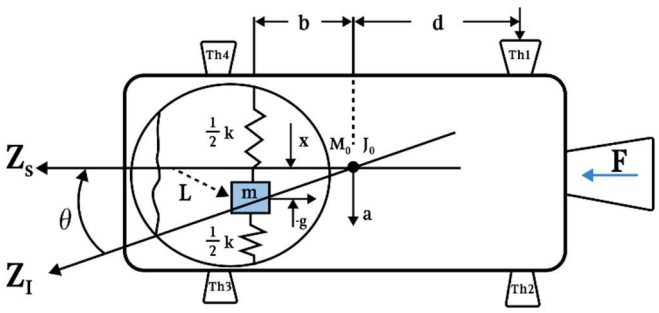

Fig 3.12: Model with one spring-mass system for writing the dynamics equation of motion.

In Fig 3.12, $\mathbf{Z_s}$ is the geometrical axis of the satellite, which is assumed to be a principal axis; $\mathbf{Z_I}$ is the inertial axis of the system before the lateral disturbance has been applied. The force **F** produces a linear acceleration that may be calculated as

$$g = \frac{F}{M_0 + m} \tag{3.18}$$

If only one thruster is fired (e.g. Thl), the applied force **f** can be divided into a linear side force **f** parallel to ***f'*** and acting on the cm of the satellite - and a torque **T** = ***f*****d** about the cm. On the other hand, the force **f**, together with **k** as in Figure 3.12, produces a lateral acceleration **a** with amplitude.

$$a = \frac{f + kx}{M_0} \tag{3.19}$$

Next, we can write the moment equation about the **cm**:

$$J_0\ddot{\theta} = df - bkx - mgx \tag{3.20}$$

$$m(a + \ddot{x} - b\ddot{\theta}) = -kx \tag{3.21}$$

We define $k_1 = bk + mg$ and $k_2 = k + \frac{mk}{M_0} = k(1 + \frac{m}{M_0})$

Then

$$J_0\ddot{\theta} + k_1 x = df \tag{3.22}$$

$$m\ddot{x} + k_2 x - mb\ddot{\theta} = -\frac{mf}{M_0} \tag{3.23}$$

Equations 3.22 and 3.23 are linear ordinary equations that can be solved with the Laplace transform

$$\begin{bmatrix} J_0 s^2 & k_1 \\ mbs^2 & -m(s^2 + k_2/m) \end{bmatrix} \begin{bmatrix} \theta(s) \\ x(s) \end{bmatrix} = \begin{bmatrix} df \\ mf/M_0 \end{bmatrix} \tag{3.24}$$

And Exactly as in the previous analysis of solar panel structural, a damping factor ξ must be incorporated into the equations of angular motion.so Eq. 3.24 be:

$$\begin{bmatrix} J_0 s^2 & k_1 \\ mbs^2 & -m\left(s^2 + 2\xi\sqrt{k_2/ms} + k_2/m\right) \end{bmatrix} \begin{bmatrix} \theta(s) \\ x(s) \end{bmatrix} = \begin{bmatrix} df \\ mf/M_0 \end{bmatrix} \tag{3.24'}$$

The solution is

$$\begin{bmatrix}\theta(s)\\ x(s)\end{bmatrix} = \frac{1}{\Delta(s)}\begin{bmatrix}-m\left(s^2 + 2\xi\sqrt{k_2/ms} + k_2/m\right) & -k_1\\ -mbs^2 & J_0 s^2\end{bmatrix}\begin{bmatrix}df\\ mf/M_0\end{bmatrix} \quad (3.25)$$

where

$$\Delta(s) = -m_0 j_0 s^2\left(s^2 + 2\xi\sqrt{k_2/ms} + k_2/m + bk_1/J_0\right) \quad (3.26)$$

Application of a Pure Torque T

In this case the example is Th1 and Th3 to achieve a positive pure moment about the **cm**, or Th2 and Th4 for a negative pure torque. So, there is no application of a side force **f,** and the transfer function becomes:

$$\frac{\theta(S)}{T(S)} = \frac{\theta(S)}{df} = \frac{s^2+2\xi\sqrt{k_2/ms}+k_2/m}{j_0 s^2\left(s^2+2\xi\sqrt{k_2/ms}+k_2/m+bk_1/J_0\right)} \quad (3.27)$$

3.7. Generalized Modeling of Structural and Sloshing Dynamics

The objective of the preceding details was to familiarize fundamental concepts of structural and sloshing dynamics. Currently, we present a complete analysis of the dynamics of a flexible spacecraft.

3.7.1. A System of Solar Panels

In the broadest scenario, a solar panel could be attached to the spacecraft using a two-axis pivoted system, allowing the module to be repositioned towards the sun from any orbital position. For the sake of simplification, we postulate that the module possesses only one degree of rotational freedom. This holds for the Spot satellite, the Hubble telescope, and all geosynchronous satellites.

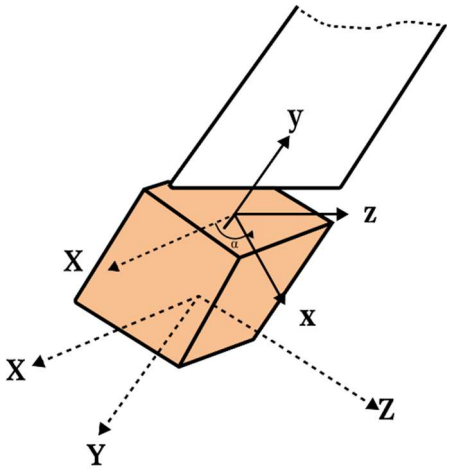

Fig 3.13: Geometry of a single-axis rotating solar panel.

3.7.2. A System of Fuel Tanks

A propulsion system may consist of several fuel tanks. With bipropellant propulsion systems, at least two tanks are mandatory. Several smaller tanks are generally preferred over a larger one to lessen the sloshing effects, although such systems are more expensive. In any case, the geometrical parameters of each tank must be defined independently of the overall spacecraft configuration. [11]

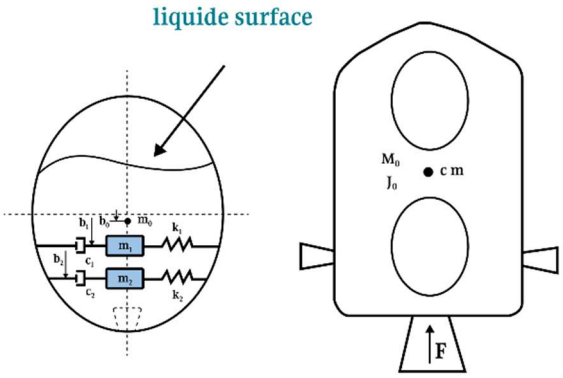

Fig 3.14: (L) Definition of the geometrical parameters of a single fuel tank and (R) the geometry of the rigid body plus two fuel tanks.

In Fig 3.14, $\mathbf{m_0}$ is the mass of the non-sloshing part of the fuel inside the tank. And $\mathbf{m_1}$, $\mathbf{m_2}$ are the two assumed sloshing masses. These three masses are distanced $\mathbf{b_0}$, $\mathbf{b_1}$ and $\mathbf{b_2}$ from a reference geometrical location. The terms $\mathbf{k_1}$ $\mathbf{k_2}$ and $\mathbf{C_1}$ $\mathbf{C_2}$ are the spring coefficients and damping parameters responsible for the damping coefficients defined in Section.

3.7.3. Complete Dynamical Modeling of Spacecraft

We assume that the translational and rotational dynamics are uncoupled. This assumption suffices to augment the dynamics of Euler's moment equations with the structural modes and sloshing dynamics in Euler's equations.

The augmented Euler equations of motion become:

$$[E]\ddot{\eta} + 2[\xi_\eta][\omega_\eta]\dot{\eta} + [\omega_\eta]^2\eta + [F]^T\ddot{\theta} = 0 \tag{3.28}$$

$$[E]\ddot{\sigma} + 2[\xi_\sigma][\omega_\sigma]\dot{\sigma} + [\omega_\sigma]^2\sigma + [B]^T\ddot{\theta} = 0 \tag{3.29}$$

where **:**

[E**] -** unit matrix (m x m) ; (n x n)

[ξ_η**]** - flexible modes damping matrix, diagonal (m x m);

[ω_η**] -** flexible modes frequency matrix, diagonal (m x m);

[F**] -** flexible coupling matrix (3 x m);

[ξ_σ**]** - sloshing modes damping matrix, diagonal (n x n) ;

[ω_σ**] -** sloshing modes frequency matrix, diagonal (m x m); and

[B**] -** flexible coupling matrix (3 x m).

3.8. Active damping control and stability analysis of flexible spacecraft

For this part, we intended to employ the state-space approach to model the flexible appendages, followed by utilizing Bode and Nichols diagrams to observe the stability of the flexible part. Subsequently, we implemented a controller to enhance the stability margins of our system.

3.8.1. State-space form

We can represent the appendage's generalized model Eq.2.28 in the state-space form as

$$\begin{cases} \dot{x} = A\,x + B\,u \\ y = C\,x + D\,u \end{cases} \tag{3.30}$$

where

$$x_1 = \eta\ ;\ x_2 = \dot{\eta}\ ; u = \ddot{\theta}$$

$$\dot{x_1} = x_2 = \dot{\eta}\ ;$$

and $$\dot{x_2} = \frac{1}{E}\left(-2\xi_\eta \omega_\eta \, x_2 \, - {\omega_\eta}^2 \, x_1\right) - \frac{F^T}{E} \, u \, ;$$

For simplification purposes we take E = 1, The equations system become:

$$\begin{bmatrix} x_1 \\ x_2 \end{bmatrix} = \begin{bmatrix} 0 & 1 \\ -{\omega_\eta}^2 & -2\xi_\eta \omega_\eta \end{bmatrix} \begin{bmatrix} x_1 \\ x_2 \end{bmatrix} + \begin{bmatrix} 0 \\ -F^T \end{bmatrix} u \qquad (3.31)$$

Accordingly, the matrices are

$$A = \begin{bmatrix} 0 & 1 \\ -{\omega_\eta}^2 & -2\xi_\eta \omega_\eta \end{bmatrix}; \quad B = \begin{bmatrix} 0 \\ -F^T \end{bmatrix}; \quad \text{D} = 0;$$

And according to [5] we take C as

$$C = [0 \quad {\varphi_r}^T] \, ;$$

where ${\varphi_r}^T$ is the appendages rotational component of mode shapes about one axis.

From the Reference [5], we select the initial three systems as instances to analyze.

Table 3.1: Nominal parameters of the flexible beam

No. System	ω_η (Hz)	ξ_η	F ($kg^{1/2}$ m)	φ_r ($kg^{-1/2}$ m^{-1})
1	1.56	0.005	-2.22	-0.706
2	9.78	0.005	-0.357	2.45
3	27.4	0.005	0.128	4.03

.

3.8.2. The controller design

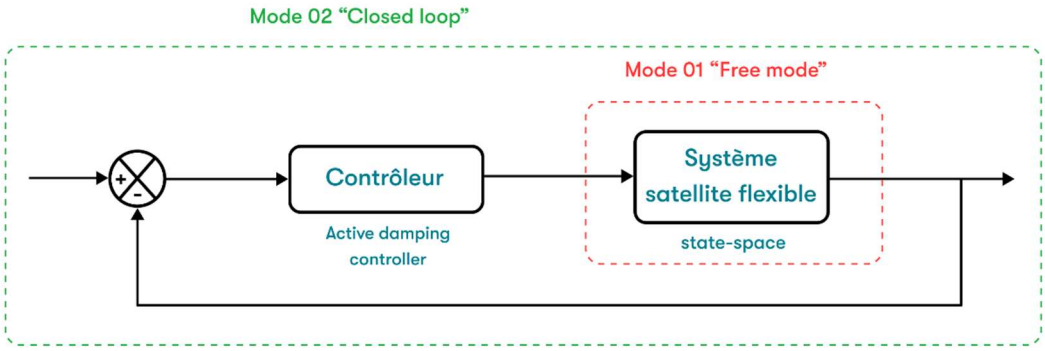

Fig 3.15: Schematic of the control loop.

As illustrated in the preceding sections, the actuator and sensor are mounted at different locations on the flexible appendage, displaying a non-collocated arrangement, which usually suggests poor stability and less robustness, in contrast to typical collocated systems. The proposed system has a dynamic feature that makes it amenable to control. It has been observed that a pair of complex conjugate poles with frequency between the first and second modes could compensate the system well, which will phase-stabilize the first two modes and gain-stabilize the higher modes simultaneously. Fig 3.15 illustrates the structure of the active damping control.

The proposed controller form is as follows:

$$C(s) = \frac{K_c}{(s^2 + 2.\xi_c.\omega_c.s + \omega_c{}^2)} \tag{3.32}$$

Table 3.2: Nominal parameters of the controller.

ω_c (rad/s)	ξ_c	K_c
36	0.707	6.7

3.8.3. Analysis of stability using Bode and Nichols plots

Employing Bode and Black diagrams with the three illustrative examples facilitates the examination of stability margins within our system. Subsequently, a precise stability assessment can be attained by applying the fundamental principles of frequency domain analysis - specifically phase and gain margins.

Secondly, the subsequent step involves integrating the controller into the system to assess its impact on stability. By implementing a feedback action per the controller's structure, we examine the bode plot. We can evaluate the stability of closed-loop systems using similar techniques employed in frequency domain analysis.

a) Mode 01 "Free mode"

System 01

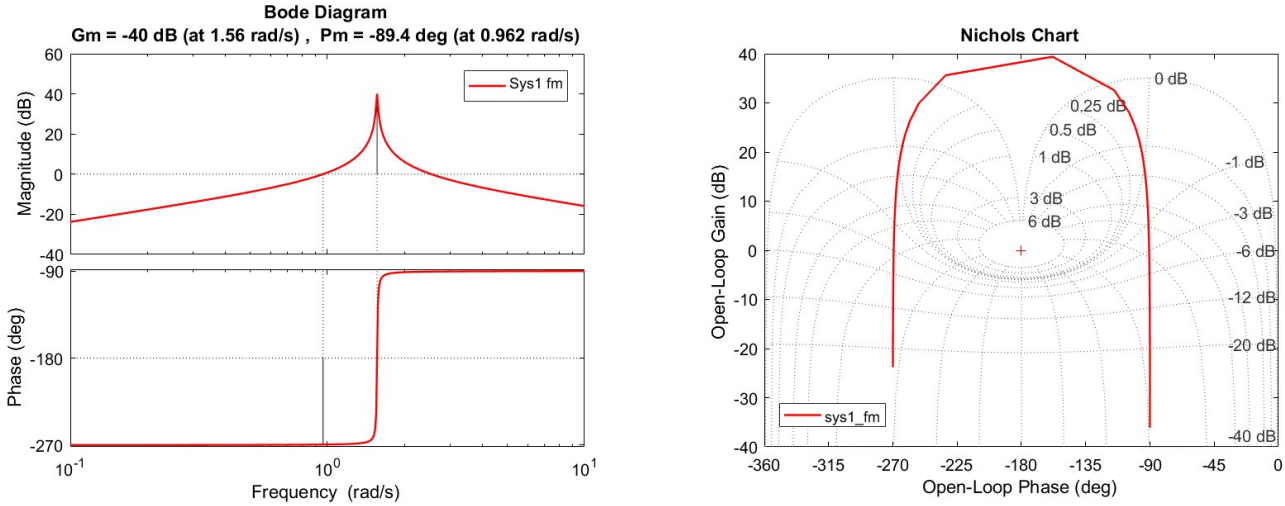

Fig 3.16: Bode and Nichols chart with margins of system 1.

The gain margin **Gm**: **- 40 dB** at ω_{c1} (pulsation at 0 dB) : **1.56 rad/s.**

The phase margin **Pm: - 89.4 °** at ω_{p1} (pulsation at -180°) : **0.962 rad/s.**

From the illustration presented in Fig 3.16, it is evident that the Nichols plot distinctly englobe the inclusion of the critical point (0 dB, -180 degrees). Based on this observation, it can be concluded that the system is unstable.

To reinforce your argument. it is observed from the Bode plot that:

$$\mathbf{Gm < 0\ ,\ Pm < 0\ \ and\ \ \omega_{p1} < \omega_{c1}}$$

According to that we can conclude that the system 01 in his free mode is unstable.

System 02

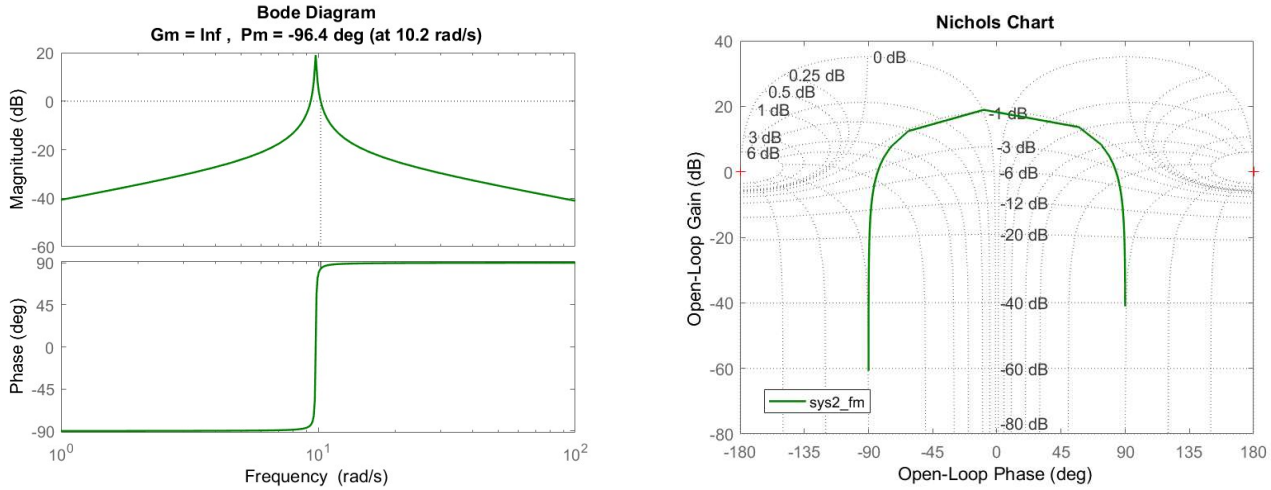

Fig 3.17: Bode and Nichols chart with margins of system 2.

The gain margin **Gm** : + ∞

The phase margin **Pm** : **- 96.4 °** at ω_{p1} (pulsation at -180°) : **10.2 rad/s.**

From the illustration presented in Fig 3.17, Nichols analysis reveals a significant deviation of
the plot trajectory from the critical point at (0 dB, -180 degrees).

To get a better statement on our argument, it is observed from the Bode plot that:

$$\mathbf{Gm > 0}\ ,\ \mathbf{Pm < 0}\ \text{ and }\ \omega_{p2} >> \omega_{c2} = 0$$

According to that we can conclude that the system 02 in his free mode is at the limits of stability.

System 03

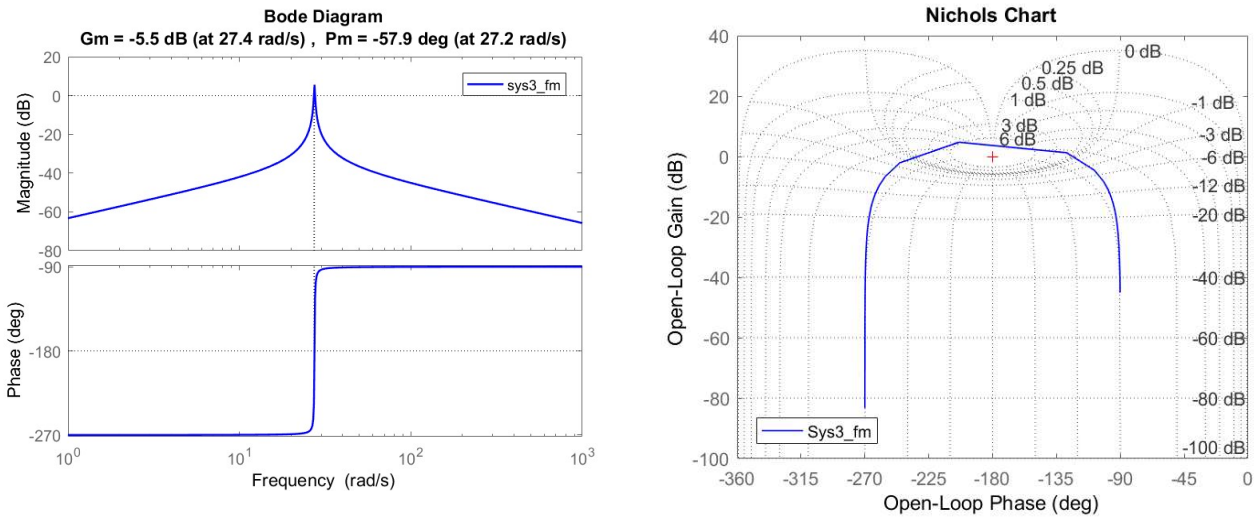

Fig 3.18: Bode and Nichols chart with margins of system 3.

The gain margin **Gm**: **- 5.5 dB** at ω_{c3} (pulsation at 0 dB): **27.4 rad/s.**

The phase margin **Pm: - 57.9 °** at ω_{p3} (pulsation at -180°) : **27.2 rad/s.**

The illustration in Fig 3.18 shows that the Nichols plot distinctly illustrates the inclusion of the critical point (0 dB, -180 degrees). Based on this observation, it can be concluded that the system is unstable. From Bode, we see that:

$$\mathbf{Gm < 0}\ ,\ \mathbf{Pm < 0}\ \text{ and }\ \omega_{p3} < \omega_{c3}$$

According to that we can conclude that the system 03 in his free mode is unstable.

b) Mode 02 “Closed loop”

System 01

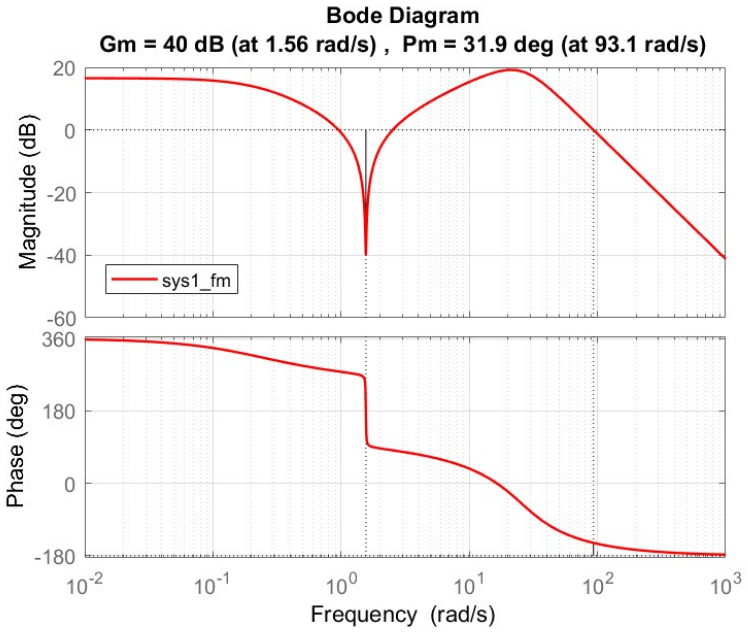

Fig 3.19: Bode and Nichols charts with margins of system 1 closed loop.

The gain margin **Gm**: **40 dB** at ω_{c1} (pulsation at 0 dB): **1.56 rad/s.**

The phase margin **Pm: 31.9 °** at ω_{p1} (pulsation at -180°): **93.1 rad/s.**

From the illustration presented in Fig 3.19, it is observed from the Bode plot of the closed loop system that:

$$\mathbf{Gm > 0,\ Pm > 0} \text{ and } \omega_{p1} < \omega_{c1}$$

Based on this analysis, we can conclude that system 01, with the controller in the closed-loop mode, is stable. Therefore, the control design's influence on system 01 is clearly evident.

System 02

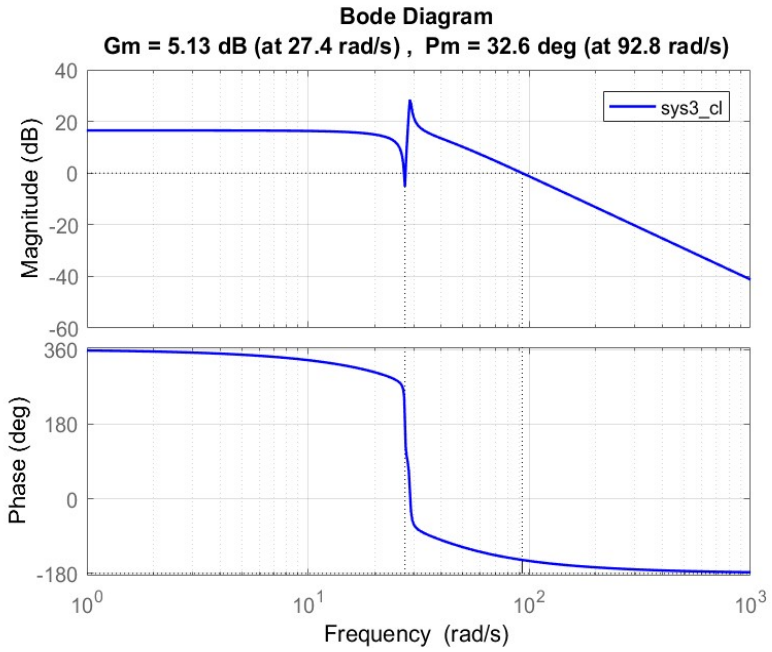

Fig 3.20: Bode and Nichols charts with margins of system 2 closed loop.

The gain margin **Gm**: + ∞. The phase margin **Pm: 33.5 °** at ω_{p2} (pulsation at -180°): **92.4 rad/s.** From the illustration presented in Figure 3.20, it is observed from the Bode plot of the closed loop system that:

$$\mathbf{Gm > 0,}\ \mathrm{Pm} > \mathbf{0}$$

The control design's influence on system 2 is observable in both the phase gain and the system's behavior.

System 03

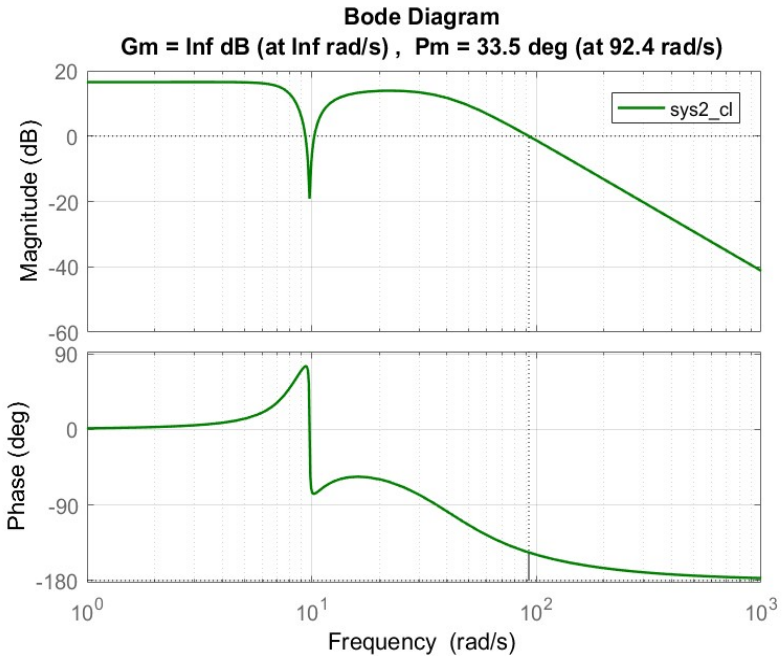

Fig 3.21: Bode and Nichols charts with margins of system 3 closed loop.

The gain margin **Gm:** 5.13 dB at $\boldsymbol{\omega}_{c3}$ (pulsation at 0 dB): **27.4 rad/s.**

The phase margin **Pm:** 32.6 ° at $\boldsymbol{\omega}_{p3}$ (pulsation at -180°): **92.8 rad/s.**

From the illustration presented in Fig 3.21, it is observed from the Bode plot of the closed loop system that:

$$\mathbf{Gm > 0, Pm > 0 \text{ and } } \boldsymbol{\omega}_{p3} < \boldsymbol{\omega}_{c3}$$

Based on this, we can conclude that system 03 with the controller in the closed-loop mode is stable. Therefore, the influence of the control design on system 03 is clearly perceivable, particularly focusing on the phase gain.

3.9. Conclusion

In this chapter, our focus is on examining the flexible appendage segment of the spacecraft, with a particular emphasis on elucidating the dynamics of solar panel motion and addressing the challenge of liquid slosh. Subsequently, we proceeded to the mathematical modeling of this flexible part by deriving the complete dynamical model of the flexible appendage, as represented in Eqs. 3.28 and 3.29. We present empirical instances of real-world flexible spacecraft models to substantiate the significance of this flexible element and its consequential impact on the overall spacecraft model. Employing stability analysis techniques, namely Bode and Nichols plots, we scrutinize the stability characteristics of each model variant. Furthermore, we employ a control design named active damping control to assess the impact of the control on the flexible segment, its effectiveness in controlling the system, and its potential to influence the overall system dynamics.

Through this exhaustive analysis, we postulate that the flexible appendage warrants meticulous consideration in spacecraft modeling. Moreover, we underscore that this flexible part can be controlled and fine-tuned through precise controller design utilizing the extracted model, as represented in Eqs.3.16, 3.27, 3.28, and 3.29.

In the next chapter, we will examine the unwanted vibration caused by flexible panels in a special case where we consider only one axis coupled with the dynamic equation of the spacecraft. Subsequently, we will apply a composite control strategy to stabilize the attitude of the flexible spacecraft.